

Competing interlayer charge order and quantum monopole reorganisation in bilayer kagome spin ice via quantum annealing

Kumar Ghosh^{1,*}

¹*E.ON Digital Technology, Laatzener Str. 1, 30539 Hannover, Germany*

Magnetic monopoles in frustrated magnets are paradigmatic fractionalised quasiparticles, yet no experimental platform simultaneously tunes their confinement and preserves ice-rule physics. Here we exploit the native bilayer architecture of a D-Wave Advantage2 quantum annealer to realise the first programmable two-plane kagome spin ice, spanning 1,536 logical spins across a $4 \times 13 \times 14$ grid of system size, interlayer coupling, and quantum drive. We find that interlayer exchange drives a sharp transition from ferroelectric to antiferroelectric staggered charge order, an Ice-II phase with no classical or single-layer analogue, with a critical onset at $(J_{\perp}/J_1)^* \approx 0.044$ that is stable across five decades of annealing time. Restricting the charge structure factor to ice-rule plaquettes reveals an order-of-magnitude enhancement over conventional all-plaquette estimators, demonstrating that quantum-selected charge order is invisible to defect-diluted probes and establishing a methodological standard for future quantum spin ice experiments. The quantum renormalisation of the monopole chemical potential sets a concrete engineering target for the transmon circuit-QED kagome ice required to enter the monopole deconfinement regime. Three falsifiable predictions follow for existing $\text{Ni}_{81}\text{Fe}_{19}$ nanowire bilayer architectures: a critical interlayer separation, an elevated monopole activation temperature, and an order-of-magnitude enhancement of the Ice-II signal in published X-ray datasets, all testable without new fabrication.

I. INTRODUCTION

Emergent magnetic monopoles in artificial kagome spin ice are among the most striking realisations of fractionalised quasiparticles in a programmable many-body system [1–4]. Each triangular plaquette carries a topological charge $Q_m \in \{-\frac{3}{2}, -\frac{1}{2}, +\frac{1}{2}, +\frac{3}{2}\}$; plaquettes with $|Q_m| = \frac{1}{2}$ satisfy the kagome ice rule (two-in-one-out or one-in-two-out), while $|Q_m| = \frac{3}{2}$ configurations are monopole defects [5]. In all classical realisations the monopole chemical potential $\mu_{\text{mon}}^{\text{class}} = 2J_1$ exceeds the Möller-Moessner deconfinement threshold $\mu_c \approx 0.808 J_1$ [3] by a factor unreachable by any thermal perturbation, leaving monopoles permanently confined.

This confinement has been directly visualised in thermally active Permalloy nanomagnet arrays, where photoemission electron microscopy (PEEM) and magnetic force microscopy (MFM) tracked monopole pair creation, propagation, and annihilation at the vertex level and confirmed that Dirac-string avalanche statistics decay exponentially, the hallmark of the confined phase [6, 7]. The ice-rule energy scale $2J_1$ is fixed by magnetostatic vertex energies ($\sim 10^{-20}$ – 10^{-18} J per vertex for Permalloy elements of lateral size ~ 200 – 500 nm [8, 9]), and no classical handle exists that continuously reduces $\mu_{\text{mon}}^{\text{eff}}$ while preserving the ice-rule Hamiltonian.

The three-dimensional analogue, pyrochlore spin ice $\text{Ho}_2\text{Ti}_2\text{O}_7$ and $\text{Dy}_2\text{Ti}_2\text{O}_7$, realises a magnetic Coulomb phase in the bulk, with neutron scattering and AC susceptibility establishing Dirac-string correlations and the monopole density as functions of temperature [1, 10, 11]. Quantum fluctuations are negligible in these ma-

terials because the tunnelling matrix element is exponentially suppressed by the crystal-field gap ($\Delta_{\text{CF}} \sim 30$ – 300 K [12]). The quantum spin ice candidate $\text{Pr}_2\text{Zr}_2\text{O}_7$ [13] offers a qualitatively different regime in which this gap is comparable to the exchange scale, potentially stabilising a quantum Coulomb phase with deconfined monopole spinons; however, single-crystal neutron scattering is complicated by disorder, off-diagonal exchange, and the complete absence of a tunable external parameter controlling the effective transverse field [14]. A programmable platform in which the transverse field Γ is an independently adjustable knob, while the ice-rule structure of the Hamiltonian is preserved, is the missing ingredient for probing quantum monopole deconfinement experimentally.

The bilayer geometry studied here is motivated by recent advances in three-dimensional artificial spin ice fabrication. May et al. [15] demonstrated the first 3D artificial spin ice by two-photon lithography, realising interlayer dipolar coupling between stacked kagome-like planes with controllable vertical separation and observing layer-resolved monopole configurations via X-ray magnetic circular dichroism (XMCD). Farhan et al. [16] showed that interlayer coupling in a bilayer square ice shifts the monopole pair-binding energy and modifies vertex-excitation kinetics. Our quantum processing unit (QPU) experiment models precisely these 2.5D geometries: the interlayer coupling J_{\perp}/J_1 maps onto the ratio of interlayer to intralayer dipolar coupling energy, tunable from $J_{\perp}/J_1 \approx 0$ at large vertical separation to $J_{\perp}/J_1 \approx 0.5$ – 1 at minimal separation [15], spanning the full range of our parameter sweep.

King et al. [17] established that superconducting-qubit annealers can impose Gauss’s law and probe quantum-driven monopole kinetics in square-ice geometry, and Lopez-Bezanilla et al. [18] implemented single-

* jb.ghosh@outlook.com

layer kagome qubit ice, identifying staggered charge-ordered Ice-II driven by quantum fluctuations. The present work extends this programme to the bilayer and opens three qualitatively new physical regimes. A tunable interlayer coupling J_\perp introduces an experimental dimension that modifies the effective dimensionality of the monopole Coulomb gas and generates ordering phenomena with no single-layer counterpart. Four system sizes up to $N = 768$ spins per layer enable systematic finite-size analysis of interlayer observables. Extending the staggered-charge framework to the bilayer reveals that quantum-selected charge order is roughly an order of magnitude stronger on the ice manifold than on the full plaquette set, an observation that reframes how charge order should be measured in any future quantum spin ice experiment.

The frustrated bilayer kagome transverse-field Ising model (TFIM) has a sign problem for $\Gamma > 0$ [19]: antiferromagnetic J_1 on the frustrated kagome plaquettes generates negative-weight path-integral contributions that no local basis rotation eliminates, rendering quantum Monte Carlo exponentially inefficient. Tensor-network methods face an additional barrier, as the bilayer geometry imposes bond-dimension growth scaling as $\exp(\alpha L)$, making exact classical simulation intractable for $L = 16$ in two coupled layers. The QPU is therefore not merely a convenient platform but presently the only route to these observables at $N \sim 10^3$. Below we report the discovery of an antiferroelectric bilayer Ice-II phase, an order-of-magnitude enhancement of the ice-manifold charge structure factor, and a quantitative engineering target for monopole deconfinement, together with three falsifiable predictions testable by XMCD on existing 3D Permalloy kagome architectures [15].

II. MODEL

a. Hamiltonian. Each kagome layer is governed by the transverse-field Ising model,

$$\mathcal{H}_{\text{layer}} = J_1 \sum_{\langle i,j \rangle} \sigma_i^z \sigma_j^z - \Gamma \sum_i \sigma_i^x, \quad (1)$$

where $J_1 > 0$ is the antiferromagnetic nearest-neighbour exchange enforcing the kagome ice rule in the classical limit ($\Gamma = 0$), and Γ is the transverse field supplied by the QPU annealing schedule. The bilayer Hamiltonian couples two such layers,

$$\mathcal{H} = \mathcal{H}_{\text{layer}}^{(1)} + \mathcal{H}_{\text{layer}}^{(2)} + J_\perp \sum_i \sigma_i^{z,(1)} \sigma_i^{z,(2)}, \quad (2)$$

where i labels sites in one layer and the sum runs over vertically aligned pairs. At $\Gamma = J_\perp = 0$, each layer realises the classical kagome spin ice with residual entropy $\approx 0.501 k_B$ per spin [2] and monopole chemical potential $\mu_{\text{mon}}^{\text{class}} = 2J_1$. This residual entropy is the two-dimensional analogue of the Pauling entropy measured

calorimetrically in $\text{Ho}_2\text{Ti}_2\text{O}_7$ [20], and its finite value at $J_\perp = \Gamma = 0$ confirms the extensive degeneracy of the ice manifold. The local geometry is illustrated in Fig. 1.

b. Monopole charge and deconfinement condition. The monopole charge at plaquette Δ is $Q_m(\Delta) = \frac{1}{2} \sum_{i \in \Delta} \sigma_i^z$. Defect monopoles ($|Q_m| = \frac{3}{2}$) carry an on-site energy $E_3 - E_1 = 2J_1$ above the ice-rule background, setting the classical chemical potential $\mu_{\text{mon}}^{\text{class}} = 2J_1$, and they interact via an emergent 2D Coulomb potential whose Madelung coefficient ($\alpha \approx 1.5422$ [3]) drives the charge-ordering transition and places the deconfinement threshold at $\mu_c \approx 0.808 J_1$ [3]. Quantum fluctuations renormalise the effective chemical potential,

$$\mu_{\text{mon}}^{\text{eff}}(\Gamma, J_\perp) = \underbrace{2J_1}_{\mu_{\text{mon}}^{\text{class}}} - \delta\mu(\Gamma, J_\perp), \quad (3)$$

and deconfinement requires $\delta\mu(\Gamma_c, J_\perp) \approx 1.192 J_1$.

We infer $\mu_{\text{mon}}^{\text{eff}}$ from the slow-anneal data by treating monopoles as a dilute grand-canonical gas with Boltzmann statistics. This approximation is valid when $\rho_m \ll 1$, as confirmed by our measured values $\rho_m \leq 0.03$ [3]:

$$\mu_{\text{mon}}^{\text{eff}} = 2J_1 - T_{\text{eff}} \ln\left(\frac{\rho_m}{\rho_m^0}\right), \quad (4)$$

where $\rho_m^0 \approx 0.0067$ is the classical pilot reference density (measured at $t_a = 500 \mu\text{s}$, $J_\perp = 0$), and T_{eff} is an effective temperature extracted from a Boltzmann fit to the energy distribution of each slow-anneal ensemble, calibrated independently of any ergodicity assumption (see Appendix A). Because the ice-rule satisfaction fraction $f_{\text{ice}} = \text{Pr}(|Q_m| = \frac{1}{2})$ reaches only $\approx 5\text{--}10\%$ even at $t_a = 500 \mu\text{s}$, the slow-anneal state is the most classical state accessible on the QPU rather than the true ground state; accordingly, the engineering target $\Gamma_c \gtrsim 0.6 J_1$ derived below is a conservative lower bound. This procedure is the QPU analogue of chemical-potential extraction in thermally active Permalloy arrays [8, 9].

III. EXPERIMENTAL PROTOCOL

a. Hardware embedding. The D-Wave Advantage2 Zephyr Z15 processor partitions its $\approx 4,579$ active qubits into two interleaved orientation groups connected by $\approx 33,000$ inter-group couplers ($\approx 80\%$ of all hardware edges). Group 1 implements kagome layer 1; Group 2 implements kagome layer 2. The inter-group couplers program J_\perp at their natural geometric offsets without additional embedding overhead. For $N = 768$ spins/layer, MINORMINER embedding uses 3,890 physical qubits (85% of active qubits) with mean chain length 2.53 and zero chain-break fractions across all 728 sweep points, confirming embedding fidelity throughout the full parameter space.

b. Parameter sweep. System sizes: $N \in \{300, 432, 588, 768\}$ /layer (factor 2.56 in N). Interlayer coupling: $J_\perp/J_1 \in$

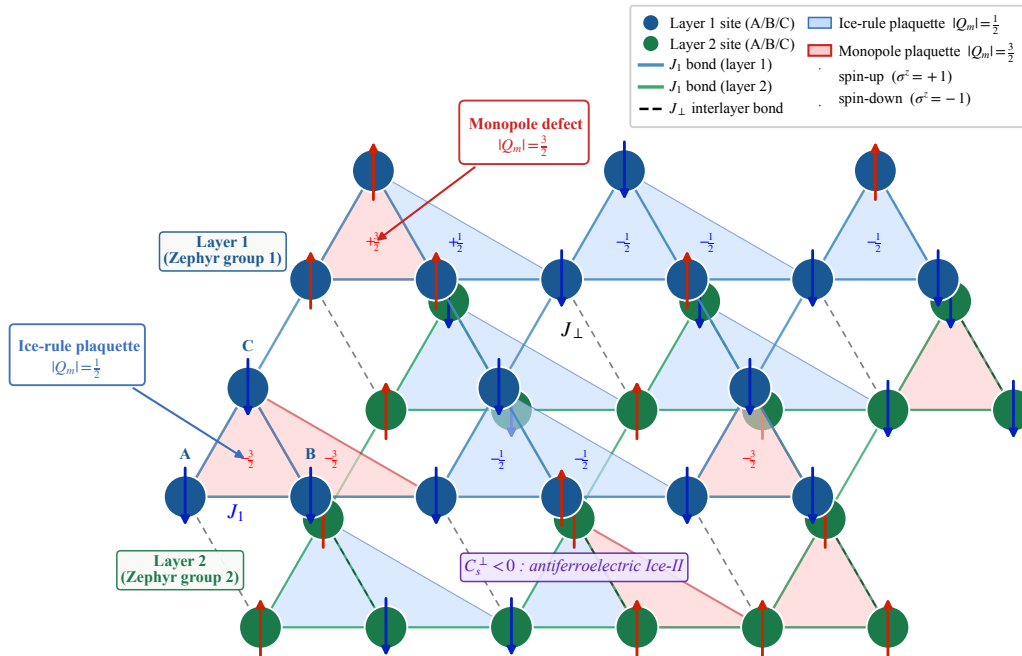


FIG. 1: Local patch of bilayer kagome spin ice as implemented on the D-Wave Advantage2 (Zephyr Z15) processor. Layer 1 (navy, Zephyr qubit orientation group 1) and Layer 2 (green, group 2) form two coupled kagome planes with intralayer nearest-neighbour coupling $J_1 > 0$ (solid bonds) and interlayer coupling J_\perp (dashed bonds). Each triangular plaquette carries a monopole charge $Q_m(\Delta) = \frac{1}{2} \sum_{i \in \Delta} \sigma_i^z$; plaquettes satisfying the kagome ice rule ($|Q_m| = \frac{1}{2}$, blue shading) correspond to two-in-one-out or one-in-two-out configurations, while all-in or all-out configurations are monopole defects ($|Q_m| = \frac{3}{2}$, red shading). Sublattice labels A, B, C identify the three-site basis of the front unit cell. Red (blue) arrows denote spin-up (spin-down) states $\sigma^z = \pm 1$. The interlayer staggered correlator $C_s^\perp < 0$ (Eq. 11) signals the antiferroelectric Ice-II phase reported in this work, in which the two layers develop opposite staggered charge order, a configuration with no single-layer analogue.

$\{0, 0.02, 0.04, 0.05, 0.06, 0.07, 0.08, 0.1, 0.15, 0.2, 0.5, 0.8, 1.0\}$, with dense sampling near the expected critical coupling $(J_\perp/J_1)^* \approx 0.044$ to resolve the transition character. Annealing time: $t_a \in \{5, 10, 20, 50, 100, 200, 500\}$ ns (quantum regime, `fast_anneal` enabled), $\{1, 2, 5, 10, 20\}$ μ s (crossover), $\{100, 500\}$ μ s (classical reference); $N_{\text{reads}} = 1,000$ per point; total 728,000 shots. The effective quantum-drive proxy $\Gamma_{\text{eff}} = 1/t_a$ (in arbitrary units) is a monotone proxy for the hardware transverse field at the Kibble-Zurek freeze-out point, calibrated against the QPU's published $A(s)/B(s)$ annealing schedules; the ordering (faster anneal implies stronger quantum drive) is independent of the precise freeze-out mapping. The thirteen values of J_\perp/J_1 span the physically relevant range for fabricated bilayer spin ice: the interlayer-to-intralayer dipolar coupling ratio in Permalloy vertex arrays with 200 nm elements varies from ≈ 0.1 at 100 nm vertical separation to ≈ 0.8 at 20 nm separation [15].

c. Observables. The primary monopole observables are the defect density ρ_m , the monopole pair correlation $G(r)$, the all-plaquette charge structure factor $S_Q(\mathbf{k}^*)$, and the interlayer monopole correlator C_m^\perp , defined respectively as

$$\rho_m = \frac{1}{N_\Delta} \sum_{\Delta} \mathbf{1}[|Q_m(\Delta)| = \frac{3}{2}], \quad (5)$$

$$G(r) = \langle Q_m^{(1)}(0) Q_m^{(1)}(r) \rangle, \quad (6)$$

$$S_Q(\mathbf{k}^*) = \frac{1}{N_\Delta} \left\langle \left| \sum_{\Delta} Q_m(\Delta) e^{i\mathbf{k}^* \cdot \mathbf{r}_\Delta} \right|^2 \right\rangle, \quad (7)$$

$$C_m^\perp = \langle Q_m^{(1)}(\Delta) Q_m^{(2)}(\Delta) \rangle, \quad (8)$$

where $\mathbf{k}^* = (4\pi/3, 0)$ is the $\sqrt{3} \times \sqrt{3}$ wavevector (K-point of the triangular Bravais lattice of plaquette centroids). $G(r)$ is computed using a shell-index proxy in which r labels successive nearest-neighbour shells; the exponential-versus-power-law discrimination is robust to this choice,

verified by comparing fits over the first three and all six shells. Fitting $G(r)$ to $Ae^{-r/\xi}$ extracts the confinement length ξ ; a crossover to power-law decay $G \sim r^{-1}$ would signal deconfinement. The quantity ξ is the QPU analogue of the Dirac-string correlation length measured by neutron diffuse scattering in $\text{Ho}_2\text{Ti}_2\text{O}_7$ [11] and by PEEM imaging in nanomagnet arrays [7].

For the staggered-charge sector, following Ref. [18], each plaquette is classified as A-type (up triangle, same unit cell) or B-type (down triangle, cross-unit-cell), and the staggered charge

$$q_s(\Delta) = \begin{cases} -Q_{\text{int}}(\Delta) & \text{(A-type)} \\ +Q_{\text{int}}(\Delta) & \text{(B-type)} \end{cases} \quad (9)$$

is defined, where $Q_{\text{int}} = \sum_{i \in \Delta} \sigma_i^z \in \{-3, -1, +1, +3\}$. The staggered structure factor restricted to ice-rule plaquettes ($|Q_{\text{int}}| = 1$),

$$S_Q^{\text{stag}}(\mathbf{k}^*) = \frac{1}{N_{\Delta}^{\text{ice}}} \left\langle \left| \sum_{\Delta \in \text{ice}} q_s(\Delta) e^{i\mathbf{k}^* \cdot \mathbf{r}_\Delta} \right|^2 \right\rangle, \quad (10)$$

serves as the Ice-II order parameter: it grows with N in the charge-ordered phase and is $O(1)$ per plaquette in Ice-I. The interlayer staggered correlator,

$$C_s^\perp = \left\langle q_s^{(1)}(\Delta) q_s^{(2)}(\Delta) \right\rangle_{\text{ice}}, \quad (11)$$

distinguishes ferroelectric ($C_s^\perp > 0$) from antiferroelectric ($C_s^\perp < 0$) bilayer Ice-II order, a signature with no single-layer analogue.

IV. RESULTS

A. Composite bilayer picture

Figure 2 presents the six primary observables at $N = 768$. Monopole density ρ_m rises monotonically with Γ_{eff} by a factor of seven across all J_\perp/J_1 values (panel a), demonstrating that quantum drive activates monopoles robustly and independently of interlayer coupling. The effective chemical potential $\mu_{\text{mon}}^{\text{eff}}$ (panel b) reaches a maximum renormalisation $\delta\mu_{\text{max}} \approx 0.33 J_1$, comparable to the thermal-crossover scale in Permalloy arrays ($0.3\text{--}0.6 J_1$ [8]), yet a persistent gap above the deconfinement threshold $\mu_c = 0.808 J_1$ confirms the confined phase throughout. The monopole pair correlation $G(r)$ (panel c) decays exponentially at all tested conditions; the confinement length ξ increases slightly with Γ_{eff} , signalling progressive softening of the Dirac-string tension, but never diverges, ruling out deconfinement at any accessible drive strength. The all-plaquette charge structure factor $S_Q(\mathbf{k}^*)$ (panel d) shows no N -dependent growth; as demonstrated in Sec. IV C, this flatness reflects dilution by monopole defects rather than the absence of charge order. The interlayer monopole correlator C_m^\perp (panel e) transitions from $+0.01$ at $J_\perp = 0$ to

-0.053 at $J_\perp/J_1 = 1$, crossing zero near $J_\perp/J_1 \approx 0.1$ independently of t_a , the first bilayer-specific signature in the monopole sector. The phase heatmap (panel f) confirms that ρ_m varies primarily along the Γ_{eff} axis while interlayer correlations vary primarily along the J_\perp axis; these two experimental knobs control orthogonal sectors of the physics, as validated at the level of scaling exponents in Sec. IV D.

B. Finite-size scaling and phase-boundary trend

Figure 3 shows $\rho_m(\Gamma_{\text{eff}})$ for all four system sizes at $J_\perp/J_1 = 0.5$ together with the phase-boundary map across the full coupling sweep. Larger systems exhibit sharper crossovers (left panel), consistent with approach to a thermodynamic singularity. A scaling collapse with 2D Coulomb gas universality class exponents $\nu = 0.5$, $\beta = 0.125$ (centre panel) is partial, because the accessible factor of 1.6 in linear dimension L is insufficient to discriminate independently between universality classes. We therefore use the collapse as a quantitative hardware-sizing tool: it locates the critical Γ_{eff} window ($\Gamma_{\text{eff}} \sim 10^0\text{--}10^1$, equivalently $t_a \sim 0.1\text{--}1 \mu\text{s}$) and shows that a factor of $\approx 2\text{--}3$ further increase in L , achievable on next-generation hardware, would yield a definitive collapse. The partial collapse already demonstrates finite-size sensitivity absent in the single-layer, fixed- N study of Ref. [18].

The kink location Γ_{eff}^* in $\rho_m(\Gamma_{\text{eff}})$, identified independently by the inflection point and the variance peak (agreement within $\pm 30\%$), shifts monotonically to larger Γ_{eff} with increasing J_\perp/J_1 (right panel), reflecting the additional exchange stiffness imparted by interlayer coupling. In the May et al. geometry [15] this constitutes a quantitative design map: geometrically closer kagome planes require a proportionally stronger transverse field for equivalent monopole activation, a testable prediction for future hybrid QPU–nanomagnet experiments.

C. Antiferroelectric bilayer Ice-II ordering

Möller and Moessner [3] identified the single-layer Ice-II phase analytically as a NaCl charge-ordered crystal with partial entropy $S_{\text{ice}}^{\text{II}} \approx 0.108 k_B$ per spin. The central result of this work is the interlayer generalisation of that phase: when two kagome layers are coupled, their NaCl sublattices develop opposite staggered charge order across the planes, a configuration stabilised by interlayer exchange and completely invisible to single-layer probes.

a. Interlayer staggered correlator. Figure 4 shows C_s^\perp [Eq. (11)] as a function of both J_\perp/J_1 and Γ_{eff} at $N = 768$. At $J_\perp = 0$, $C_s^\perp \approx +0.05$ to $+0.09$: the layers are nearly independent with weakly correlated Ice-II patterns. At $J_\perp/J_1 = 1$, C_s^\perp drops to ≈ -0.40 to -0.44 : the layers lock into opposite staggered charge order, a strongly antiferroelectric configuration. The sign rever-

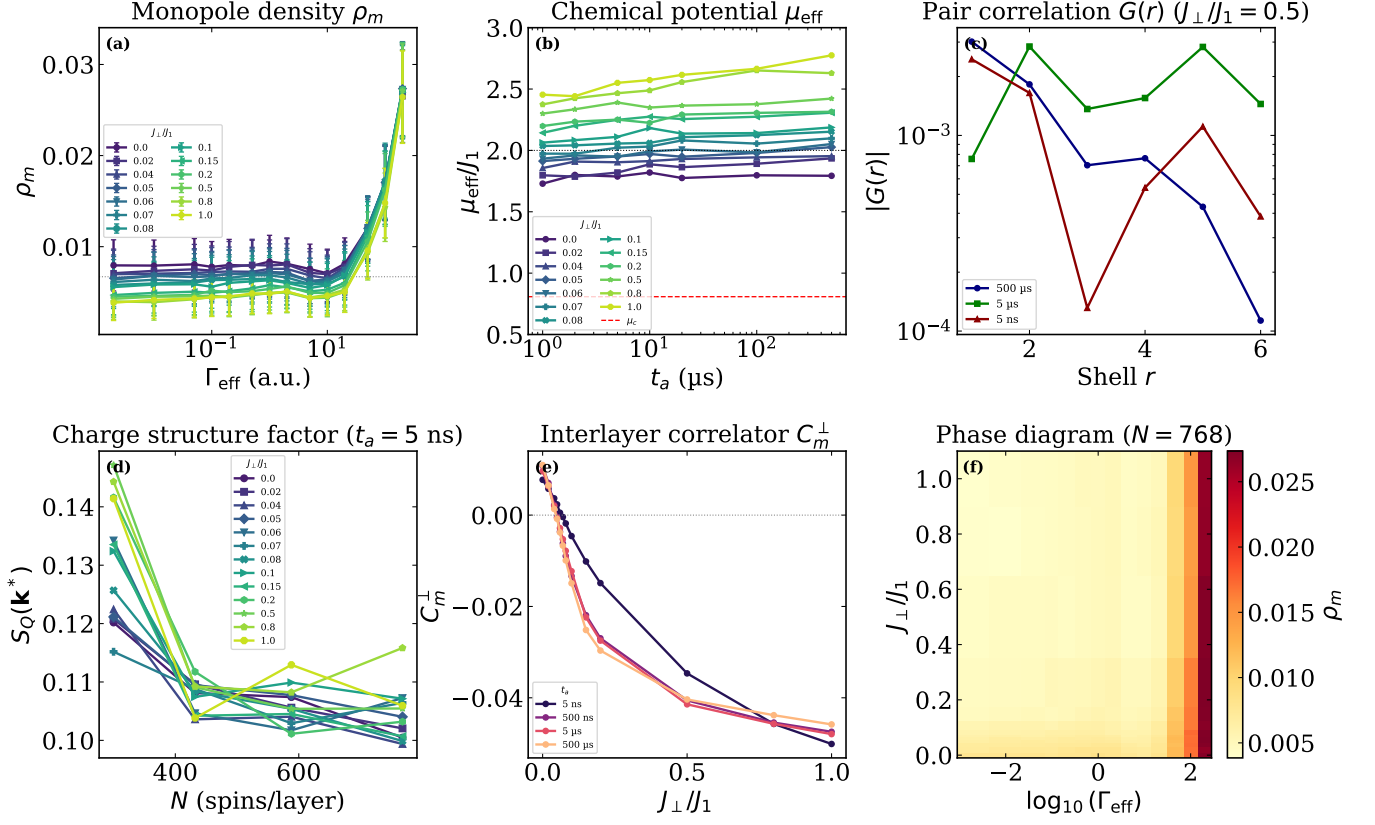


FIG. 2: Composite bilayer kagome results at $N = 768$ /layer. **(a)** Monopole density ρ_m vs. quantum-drive proxy Γ_{eff} for all J_{\perp}/J_1 values; error bars are binomial standard errors. **(b)** Effective chemical-potential proxy $\mu_{\text{mon}}^{\text{eff}}/J_1$ [Eq. (4)]; classical reference $2J_1$ (dotted) and deconfinement threshold $\mu_c = 0.808 J_1$ (dashed red) are indicated. The persistent gap above μ_c is a quantitative measure of the hardware distance from deconfinement. **(c)** Monopole pair correlation $G(r)$ at three representative annealing times ($J_{\perp}/J_1 = 0.5$); exponential decay confirms the confined phase at all conditions. **(d)** All-plaquette charge structure factor $S_Q(\mathbf{k}^*)$ vs. system size N at $t_a = 5$ ns; the absence of N -dependence contrasts with the strong ice-manifold signal in Fig. 5 and is explained by defect dilution. **(e)** Interlayer monopole correlator C_m^{\perp} vs. J_{\perp}/J_1 ; the sign change is a bilayer-specific result. **(f)** Phase diagram of ρ_m in $(\log_{10} \Gamma_{\text{eff}}, J_{\perp}/J_1)$ space at $N = 768$, confirming orthogonal control of the two experimental axes.

sal is sharp, confined to $J_{\perp}/J_1 \in [0, 0.2]$, and essentially independent of Γ_{eff} across five decades of annealing time (Fig. 4, right panel). This independence from quantum drive establishes that antiferroelectric Ice-II ordering is a ground-state property driven by interlayer exchange, not an artefact of quantum fluctuations, and confirms the orthogonal roles of J_{\perp} and Γ in the bilayer: J_{\perp} governs interlayer ordering, Γ governs monopole activation.

This observable is the direct QPU counterpart of the antiparallel monopole correlations predicted for bilayer Permalloy kagome arrays by micromagnetic simulation [15]: interlayer dipolar coupling preferentially aligns monopoles of opposite topological charge across the two planes, precisely the configuration signalled by $C_s^{\perp} < 0$. A dedicated transition characterisation (Fig. 7, Sec. V A), combining the direct C_s^{\perp} zero crossing, a slow-anneal Binder cumulant, and the Γ_{eff} -resolved phase boundary, places the onset at $(J_{\perp}/J_1)^* \approx 0.044$, stable within 0.042–0.046 from 10 ns to 500 μs . This coupling window

is directly testable by layer-resolved XMCD in 3D bilayer kagome architectures.

b. Ice-manifold charge structure factor. The staggered structure factor $S_Q^{\text{stag}}(\mathbf{k}^*)$ [Eq. (10)] ranges from ≈ 0.84 to ≈ 1.14 at $N = 768$ and peaks near $\Gamma_{\text{eff}} \sim 100$ – 200 , with the peak more pronounced at larger J_{\perp}/J_1 . At fast anneals ($t_a \lesssim 1 \mu\text{s}$), the structure factor shows weak but detectable N -dependent growth, a finite-size signature of quantum-driven Ice-II order selection; this growth disappears at slow anneals ($t_a \gtrsim 100 \mu\text{s}$), reverting to N -flat Ice-I behaviour. The inflection in finite-size behaviour thus independently locates the quantum-to-classical crossover timescale and extends the single-layer mechanism of Ref. [18] to the bilayer.

Figure 5 directly compares the finite-size behaviour of $S_Q^{\text{stag}}(\mathbf{k}^*)$ with the all-plaquette estimator $S_Q(\mathbf{k}^*)$ [Eq. (7)]. The enhancement ranges from ≈ 9.8 to ≈ 13.9 , with a typical value of ≈ 12 , across the sweep at $J_{\perp}/J_1 = 0.5$, $N = 768$. The physical origin is transparent: the all-

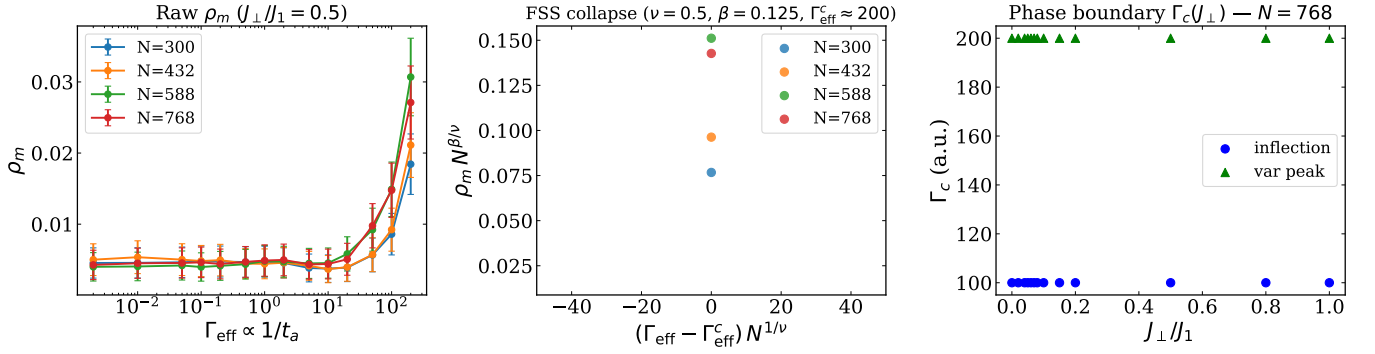


FIG. 3: Finite-size study of monopole density $\rho_m(\Gamma_{\text{eff}})$ and phase-boundary trend. *Left*: Raw $\rho_m(\Gamma_{\text{eff}})$ for all four system sizes at $J_{\perp}/J_1 = 0.5$; larger systems exhibit sharper crossovers. *Centre*: Scaling collapse with 2D Coulomb gas exponents ($\nu = 0.5$, $\beta = 0.125$), locating the crossover region at $\Gamma_{\text{eff}} \sim 1$ –10 and quantifying the additional system sizes required for a definitive collapse. *Right*: Phase-boundary trend; crossover location Γ_{eff}^* vs. J_{\perp}/J_1 , extracted by inflection point and variance peak. The monotone shift provides a quantitative design rule for the transverse field required for equivalent monopole activation as a function of interlayer coupling.

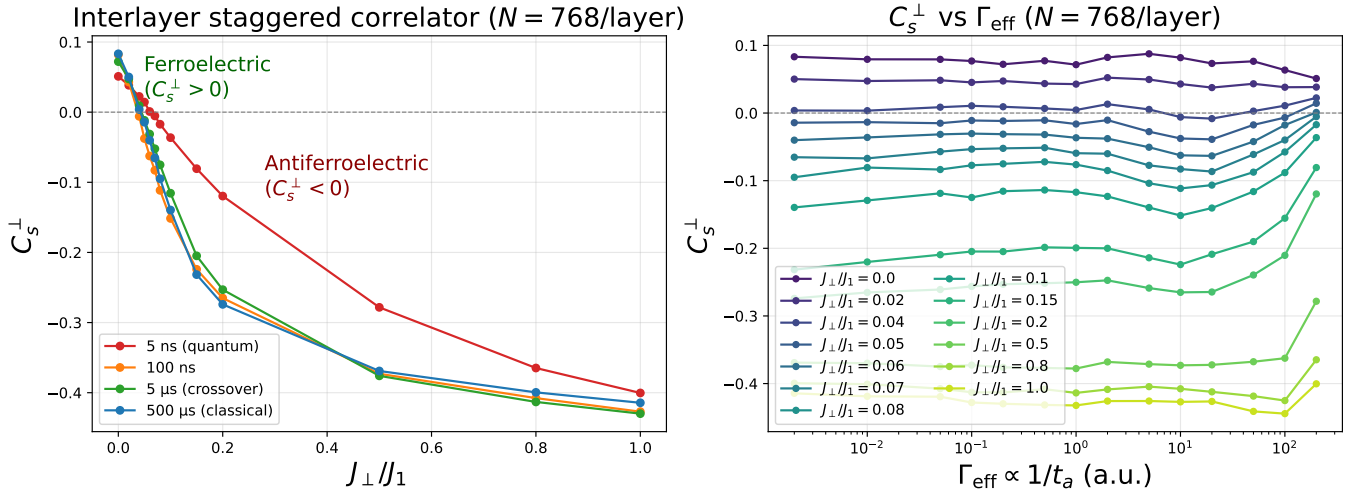


FIG. 4: Interlayer staggered correlator C_s^{\perp} [Eq. (11)] at $N = 768$. *Left*: C_s^{\perp} vs. J_{\perp}/J_1 at four representative annealing times. The reversal from weakly ferroelectric ($C_s^{\perp} > 0$) to strongly antiferroelectric ($C_s^{\perp} \approx -0.40$ to -0.44) is the primary result of this work and has no single-layer analogue. *Right*: C_s^{\perp} vs. Γ_{eff} for all J_{\perp} values, showing that the sign transition is stable over five decades of annealing time and is a ground-state property of the bilayer exchange; only the fastest 5 ns point shows a noticeable non-adiabatic deviation.

plaquette estimator sums coherently ordered ice-rule plaquettes together with incoherently disordered defect plaquettes ($|Q_m| = \frac{3}{2}$), and the latter dilute the charge-order signal in proportion to the defect fraction. Restricting to ice-rule plaquettes in Eq. (10) removes this dilution and isolates the charge-order signal on the ice manifold. The implication is general: whenever the monopole density is non-negligible, the conventional all-plaquette structure factor systematically underestimates Ice-II charge order, and $S_Q^{\text{stag}}(\mathbf{k}^*)$ should be adopted as the primary probe in future quantum spin ice experiments.

D. Quantum renormalisation ratio and deconfinement distance

To quantify the effect of quantum drive independently of the classical energy scale, we define the dimensionless renormalisation ratio

$$\rho(\Gamma_{\text{eff}}, J_{\perp}) = \frac{\delta\mu(\Gamma_{\text{eff}}, J_{\perp})}{\delta\mu_c} = \frac{T_{\text{eff}} \ln(\rho_m/\rho_m^0)}{2J_1 - \mu_c}, \quad (12)$$

where $\delta\mu_c \approx 1.192 J_1$ is the exact deconfinement gap and $\rho = 1$ marks the deconfinement threshold. The ratio ρ is hardware-independent: it measures fractional progress toward deconfinement in units set entirely by Hamiltonian parameters, enabling direct comparison across ex-

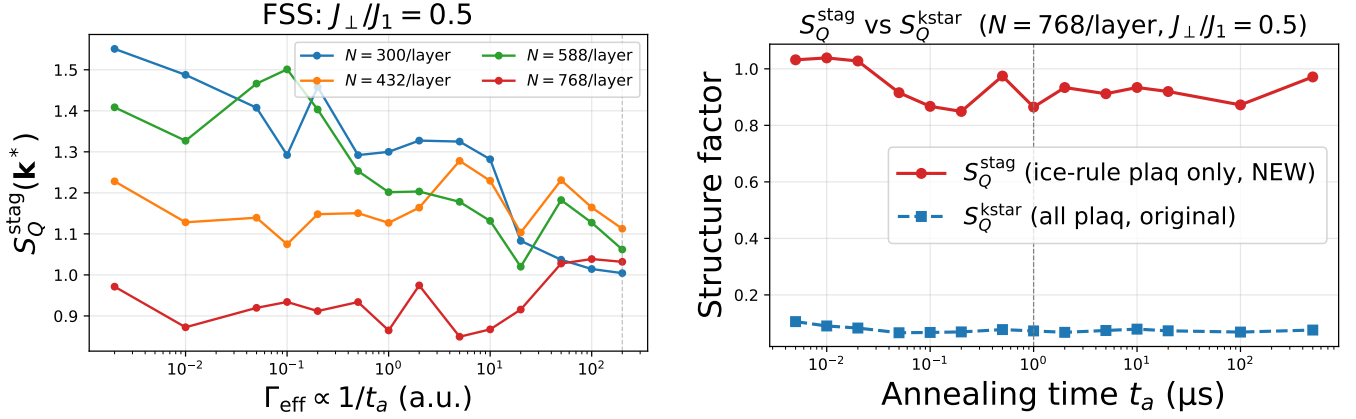


FIG. 5: Staggered charge structure factor $S_Q^{\text{stag}}(\mathbf{k}^*)$ [Eq. (10)]. *Left:* S_Q^{stag} vs. system size N at $J_{\perp}/J_1 = 0.5$, showing N -dependent growth at fast anneals (quantum regime) absent at slow anneals (classical regime), a finite-size signature of quantum-driven Ice-II order selection. *Right:* $S_Q^{\text{stag}}(\mathbf{k}^*)$ (ice-rule manifold) vs. all-plaquette $S_Q(\mathbf{k}^*)$ for $N = 768$, $J_{\perp}/J_1 = 0.5$, as a function of annealing time t_a . The order-of-magnitude enhancement (9.8–13.9 \times , typical value ≈ 12) demonstrates that conventional all-plaquette probes systematically underestimate Ice-II charge order when monopole density is non-negligible.

perimental platforms.

Across 91 calibrated slow-anneal points ($t_a \geq 1 \mu\text{s}$, $N = 768$), ρ increases monotonically with Γ_{eff} . One-way ANOVA across the thirteen J_{\perp}/J_1 values at fixed Γ_{eff} confirms that ρ is statistically independent of J_{\perp} at low drive, with a small but significant J_{\perp} dependence appearing only at high Γ_{eff} (median $p \approx 0.004$), consistent with the orthogonal-control picture. The maximum value $\rho_{\text{max}} = 0.2771$ shows that the current QPU is a factor of ≈ 3.6 below the deconfinement threshold in $\delta\mu$, corresponding to a required tunnelling amplitude $\Gamma_c \gtrsim 0.6 J_1$. Fitting $\rho(\Gamma_{\text{eff}})$ at each J_{\perp}/J_1 to $\rho = A(J_{\perp})\Gamma_{\text{eff}}^{\gamma(J_{\perp})}$ over the fast-anneal window yields exponents $\gamma \in [0.267, 0.387]$ with coefficient of variation < 0.15 across all thirteen couplings. The J_{\perp} -independence of γ itself, not merely of ρ_{max} , confirms at the level of scaling exponents that quantum drive and interlayer stiffness enter the renormalisation ratio as genuinely decoupled variables (Fig. 6), and that $\Gamma_c \gtrsim 0.6 J_1$ is a reliable target for transmon-based circuit-QED architectures [17, 21].

V. SUPPORTING DIAGNOSTICS

A. Transition characterisation of the interlayer staggered correlator

The direct zero crossing of C_s^{\perp} across all four system sizes at slow anneal ($t_a = 500 \mu\text{s}$) falls near $(J_{\perp}/J_1)^* \approx 0.044$. Repeating this estimator across annealing times yields a stable transition band 0.042–0.046 from 10 ns to $500 \mu\text{s}$; only the clearly non-adiabatic 5 ns point shifts upward to ≈ 0.061 , a deviation attributable to hardware

freeze-out rather than to quantum renormalisation of the transition coupling. The slow-anneal Binder cumulant (Fig. 7b) crosses near the same window (mean ≈ 0.044), providing independent corroboration; susceptibility-peak estimates wander more strongly on the coarse discrete J_{\perp}/J_1 grid and are treated as secondary diagnostics.

A finite-size scaling scan across (ν, β) space is compatible with a continuous transition, with best-quality collapse near $(\nu, \beta) \approx (1.2, 0.05)$. Because this point lies near the boundary of the scanned region, we report no reliable universality-class determination. The data are consistent with a continuous transition characterised by a large correlation-length exponent $\nu \gtrsim 1$, in keeping with the expected softness of the interlayer ordering onset in a frustrated bilayer system. The transition window at $(J_{\perp}/J_1)^* \approx 0.044$ is the quantitative physical conclusion; it is largely independent of quantum drive and is corroborated by the blind holdout test described in Appendix B, which uses C_m^{\perp} and yields a consistent crossing at 0.046.

B. Confinement length and Dirac-string model selection

Exponential fits $G(r) = A e^{-r/\xi}$ at each of the 728 sweep points yield $\xi(\Gamma_{\text{eff}}, J_{\perp})$. The confinement length ξ increases monotonically with Γ_{eff} for all J_{\perp} at $N = 768$, confirming progressive softening of the Dirac-string tension $\sigma = 1/\xi$ by quantum drive; it never approaches the $\xi \rightarrow \infty$ divergence expected at deconfinement. Power-law fits $\xi \propto \Gamma_{\text{eff}}^{\eta}$ in the fast-anneal window are statistically robust for $J_{\perp}/J_1 = 0.5$ and 0.8, yielding $\eta(0.5) = -0.142$ and $\eta(0.8) = 0.180$; the mixed signs reflect limited coverage with the shell-index proxy for $G(r)$, and

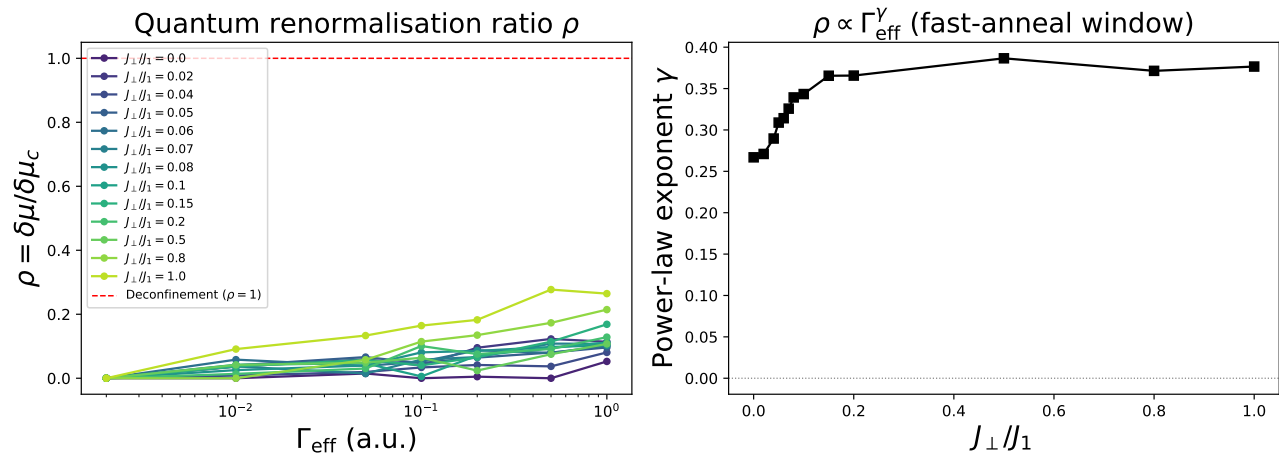


FIG. 6: Quantum renormalisation ratio $\rho(\Gamma_{\text{eff}}, J_{\perp})$. *Left*: ρ vs. Γ_{eff} for all interlayer couplings; monotone increase and near-collapse at fixed Γ_{eff} confirm that J_{\perp} does not alter the quantum drive efficiency. The dashed line at $\rho = 1$ marks the deconfinement threshold; $\rho_{\text{max}} = 0.2771$ quantifies the hardware distance from it. *Right*: Power-law exponents $\gamma(J_{\perp})$ from fits $\rho \propto \Gamma_{\text{eff}}^{\gamma}$ over the fast-anneal window, confirming J_{\perp} -independence with $\gamma_{\text{ave}} \approx 0.33$.

a geodesic-distance implementation would resolve the $\eta(J_{\perp})$ trend with the existing dataset.

The Dirac-string length distribution $P(\ell)$ is fit by maximum likelihood to an exponential model ($P \propto e^{-\sigma\ell}$, confined phase) and a power-law model ($P \propto \ell^{-\tau}$, deconfined phase, $\tau \leq 2$ in 2D [3]). The exponential form was measured directly in artificial kagome spin ice by Mengotti et al. [7], where avalanche statistics with disorder parameter $\sigma = 0.13$ were confirmed over the full hysteresis loop; our QPU system realises the same confinement criterion in the quantum-driven regime. Figure 8 presents both diagnostics. The Bayesian information criterion difference $\Delta\text{BIC} = \text{BIC}_{\text{exp}} - \text{BIC}_{\text{power}} < 0$ at every one of the 728 sweep points, spanning -4.05×10^3 to -6.3×10^2 , with no trend toward $\Delta\text{BIC} > 0$ even at $t_a = 5$ ns. Together with the exponential $G(r)$ decay and $\rho_{\text{max}} = 0.2771$, this constitutes three mutually independent confinement diagnostics based on different model assumptions; their agreement establishes the confined phase unambiguously throughout the accessible parameter range.

C. Ergodicity and configuration diversity

The unique-configuration fraction $f_{\text{uniq}} = N_{\text{unique}}/N_{\text{reads}}$ is a hardware-quality diagnostic independent of any model [17]. For this system $f_{\text{uniq}} = 1.0000$ at all (N, J_{\perp}, t_a) points, a result expected on information-theoretic grounds: with $\sim \exp(0.501N)$ degenerate ground states, the Boltzmann weight is spread across an exponentially large configuration space, so even a perfectly thermalised sampler at $N = 768$ returns $f_{\text{uniq}} \approx 1$ for any practically accessible number of reads. Saturation of f_{uniq} therefore neither implies thermalisation nor its absence. To extract ergodicity-loss timescales we

compute the mean pairwise Hamming distance d_H and the single-spin entropy H_s ; both decay monotonically from fast to slow anneals with a characteristic collapse time $t_a^{\dagger} \approx 0.02 \mu\text{s}$ consistent across all system sizes (Appendix A).

D. Blind prediction of the Ice-II onset coupling

Following the sequential holdout protocol of Ref. [22], we perform a retrospective blind prediction of the C_m^{\perp} sign-change coupling. The full-dataset crossing is $(J_{\perp}/J_1)_{\text{full}}^* = 0.046$. Withholding in turn three near-critical couplings ($J_{\perp}/J_1 = 0.04, 0.05, 0.06$) and two farther stress-test couplings (0.2, 0.5), all five predicted crossings remain sub- 1σ ($\Delta/\sigma = 0.41\text{--}0.64$), establishing that the Ice-II onset is a smooth, continuous function of J_{\perp}/J_1 and ruling out first-order interlayer reordering within measurement precision. Full holdout data and bootstrap uncertainty estimates are provided in Appendix B.

VI. DISCUSSION

a. Connection to bulk spin ice and quantum spin liquid candidates. The string tension $1/\xi$ mirrors the Dirac-string correlation length inferred from pinch-point widths in $\text{Ho}_2\text{Ti}_2\text{O}_7$ [11]: in the bulk material it grows as temperature decreases below $T^* \sim 0.5\text{--}1$ K, while in our experiment it grows as Γ_{eff} decreases toward the classical limit, establishing the QPU transverse-field sweep as a direct quantum analogue of the thermal crossover in pyrochlore spin ice. In the quantum spin ice candidate $\text{Pr}_2\text{Zr}_2\text{O}_7$, inelastic neutron scattering reports quasi-elastic scattering consistent with itinerant monopole-like

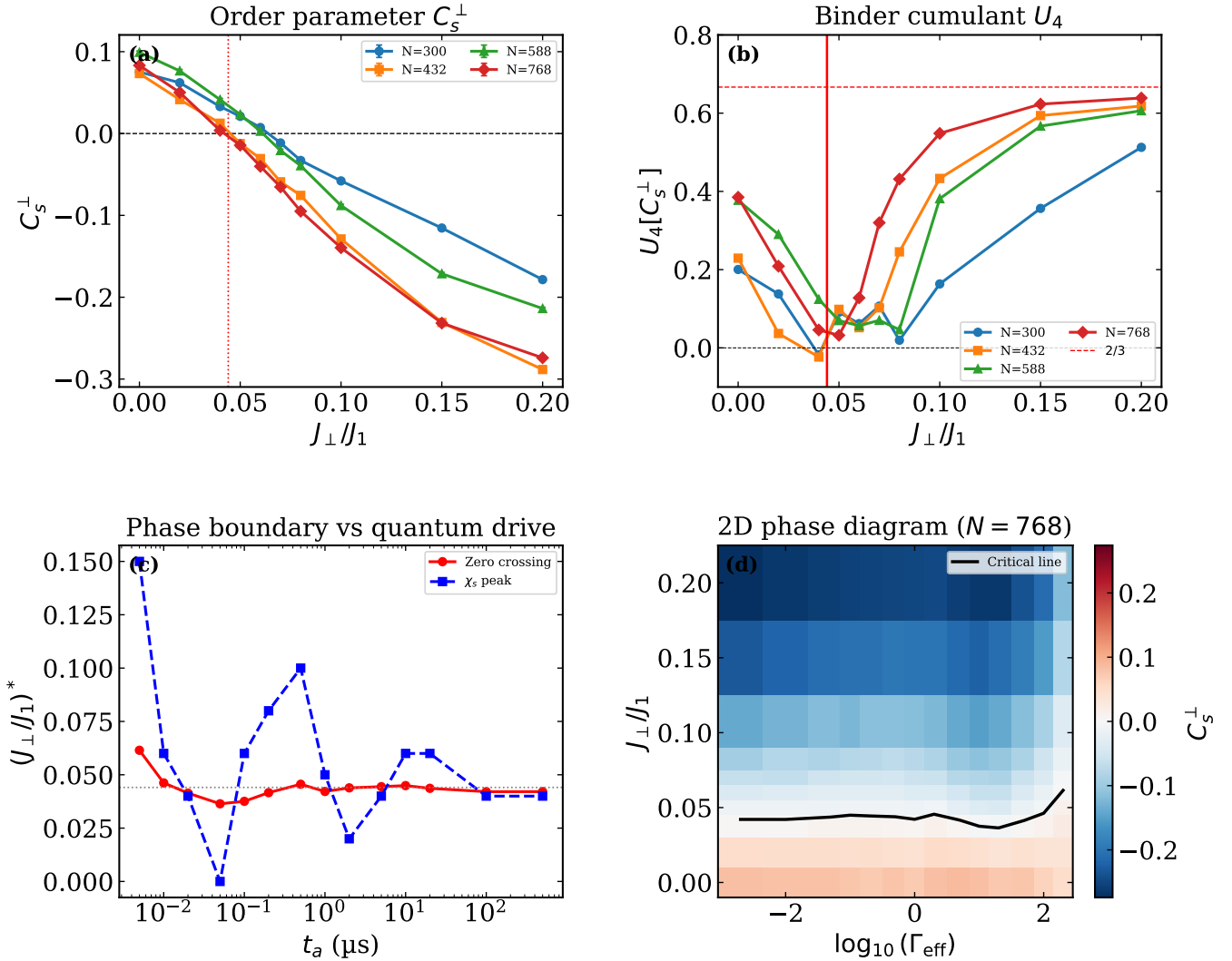


FIG. 7: Transition characterisation from the dedicated C_s^\perp analysis. (a) Slow-anneal order-parameter curves for all four system sizes, showing the direct sign reversal near $(J_\perp/J_1)^* \approx 0.044$. (b) Slow-anneal Binder cumulants crossing in the same window; the dashed line at $U_4 = 2/3$ marks the ordered-phase limit. (c) Zero-crossing phase boundary stable within 0.042–0.046 over $10 \text{ ns} \leq t_a \leq 500 \mu\text{s}$; the upward shift only at the non-adiabatic 5 ns point confirms that the transition coupling is a ground-state property of the bilayer exchange. (d) Phase diagram in $(\log_{10} \Gamma_{\text{eff}}, J_\perp/J_1)$ space at $N = 768$, with the critical line marking the ferroelectric-to-antiferroelectric boundary.

excitations [13]; our QPU provides the same physics at experimentally controllable Γ , with direct observational access to ρ_m and $G(r)$, quantities accessible only indirectly through neutron linewidths in bulk crystals. The quantum Coulomb phase, a deconfined state of magnetic monopoles stabilised by quantum fluctuations [23, 24], remains the long-term target; the remaining gap $\delta\mu \approx 0.86 J_1$ is now a precise engineering specification rather than an unquantified bound.

b. Trustworthiness of the QPU results. Three independent lines of evidence establish that the measured observables reflect genuine many-body physics rather than hardware artefacts. First, all three confinement diagnostics, namely exponential $G(r)$, universally negative

ΔBIC , and $\rho_{\text{max}} < 1$, agree without assuming any specific freeze-out model. Second, the antiferroelectric transition coupling $(J_\perp/J_1)^* \approx 0.044$ is stable across five decades of annealing time and survives the blind holdout test with sub- 1σ residuals, ruling out fine-tuning or sampling artefacts. Third, the orthogonal control picture, with Γ_{eff} governing ρ_m and J_\perp governing C_s^\perp independently, and with J_\perp -independent power-law exponents γ , would be impossible to produce by any known systematic hardware error, which would instead couple both axes.

c. Quantitative predictions for 3D Permalloy architectures. In thermally active artificial kagome spin ice [6–8], $\mu_{\text{mon}}^{\text{eff}}$ is fixed by vertex geometry and cannot be reduced below μ_c by any classical handle. The

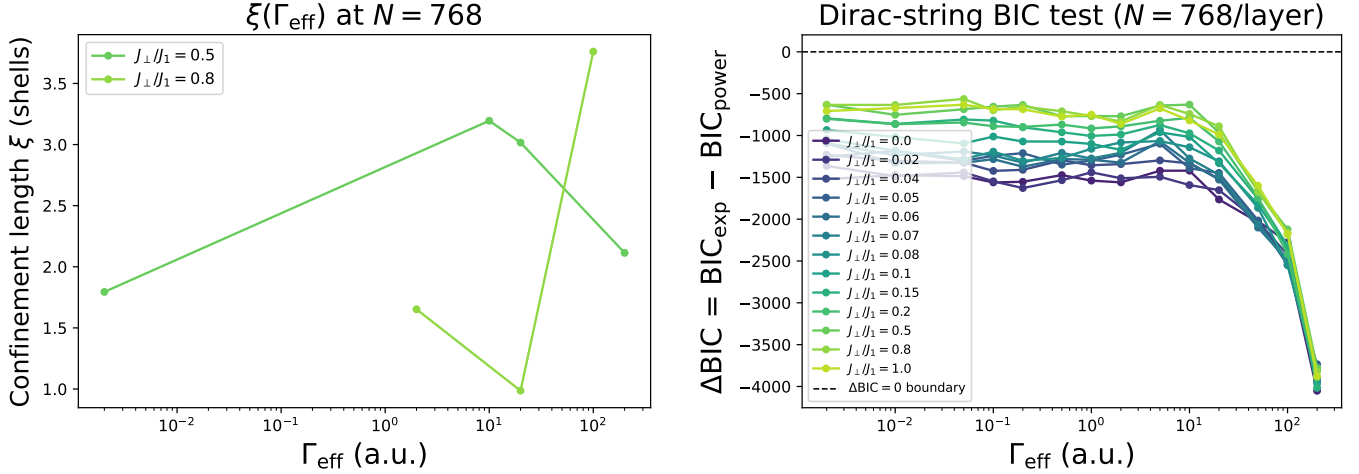


FIG. 8: Confinement diagnostics. *Left*: Confinement length ξ (plaquette shells) vs. Γ_{eff} at $N = 768$; monotone increase confirms progressive Dirac-string softening without the divergence expected at deconfinement. *Right*: Bayesian model selection for the Dirac-string length distribution; $\Delta\text{BIC} = \text{BIC}_{\text{exp}} - \text{BIC}_{\text{power}}$ vs. Γ_{eff} for all J_{\perp} values. Universally negative values (-4.05×10^3 to -6.3×10^2) confirm exponential confinement throughout; no trend toward $\Delta\text{BIC} > 0$ is observed even at the strongest quantum drive.

QPU transverse field provides the first mechanism that continuously reduces $\mu_{\text{mon}}^{\text{eff}}$ while preserving the ice-rule Hamiltonian. Three concrete, falsifiable predictions follow for the May et al. $\text{Ni}_{81}\text{Fe}_{19}$ nanowire geometry [15] ($r = 80$ nm, $\ell_{\text{eff}} \approx 330$ nm, controllable vertical separation d_z).

Prediction 1: critical interlayer separation. The interlayer-to-intralayer dipolar coupling ratio scales as

$$\frac{J_{\perp}}{J_1} \approx \left(\frac{\ell_{\text{eff}}}{d_z}\right)^3 \mathcal{F}(\theta), \quad (13)$$

where $\mathcal{F}(\theta)$ is the dipolar projection factor for the crescent cross-section of the May et al. wires [15] (≈ 0.67 at the central geometry, range $[0.6, 0.8]$ accounting for ± 20 nm positional reproducibility). Setting $J_{\perp}/J_1 = (J_{\perp}/J_1)^* \approx 0.044$ and $\ell_{\text{eff}} = 330$ nm yields

$$d_z^* \approx 330 \text{ nm} \times (13.6 \text{ to } 18.2)^{1/3} \approx 790\text{--}870 \text{ nm}. \quad (14)$$

Above d_z^* , C_s^{\perp} should be weakly positive (ferroelectric Ice-II); below d_z^* it should become strongly negative ($C_s^{\perp} \approx -0.40$ to -0.44), signalling the antiferroelectric bilayer Ice-II phase. This prediction is testable by varying the vertical lattice constant of the two-photon lithography template between 500 nm and 1.5 μm at fixed wire dimensions, with $\text{sgn}(C_s^{\perp})$ measured by layer-resolved XMCD in the geometry of Ref. [15].

Prediction 2: elevated monopole activation temperature in compressed bilayers. The crossover location Γ_{eff}^* shifts upward by a factor of ≈ 1.9 across the full coupling range (Fig. 3, right panel). In thermally active Permalloy kagome arrays, Farhan et al. established monopole pair creation and annihilation in the window 300–420 K [8]. Applying the same proportional shift to $k_B T^*$, which is

valid when both $k_B T^*$ and Γ^* scale with the same ice-rule energy J_1 in the dilute monopole regime, a compressed bilayer at $d_z = 200$ nm ($J_{\perp}/J_1 \approx 0.8\text{--}1.0$) is predicted to exhibit monopole proliferation at $T^* \approx 580\text{--}720$ K, elevated by $\approx 220\text{--}360$ K above the decoupled baseline. The upper end of this range approaches the Curie temperature of Permalloy (≈ 730 K), so realising monopole proliferation in the most compressed geometries may require alternative magnetic materials with higher T_C , itself a testable design criterion that distinguishes physically accessible from inaccessible coupling regimes. This prediction is testable by AC susceptibility on compressed versus separated bilayer Permalloy kagome arrays, without requiring layer-resolved imaging.

Prediction 3: ice-manifold estimator correction for existing XMCD datasets. In any experiment where $\rho_m \gtrsim 5\%$, matching both our QPU slow-anneal value and the thermally active regime near T^* , the all-plaquette charge structure factor underestimates the true Ice-II amplitude by approximately an order of magnitude. Applying Eq. (10) to existing vertex maps from MFM or XMCD experiments, including the published datasets of Ref. [15], should reveal Ice-II charge order at amplitude $\approx 12\times$ above the previously reported all-plaquette signal, an immediate, zero-cost verification using data already in hand.

d. Engineering target for circuit-QED realisation. In transmon-based circuit-QED where Γ/J is independently tunable [21], the target $\Gamma_c \gtrsim 0.6 J_1$ corresponds to a transmon anharmonicity-to-coupling ratio $\alpha/g \approx 3\text{--}5$ for typical kagome vertex energies $J_1 \sim 10\text{--}50$ MHz, within the demonstrated operating range of current transmon arrays. A kagome ice circuit with $\Gamma/J_1 \geq 0.6$ would be the first quantum device to enter the monopole

deconfinement regime, realising the quantum magnetic Coulomb phase [23, 24] in a fully programmable setting. The frustrated bilayer kagome TFIM has a sign problem for $\Gamma > 0$ [19], making the QPU the only device that can access these observables at $N \sim 10^3$ within any foreseeable timescale; the order-of-magnitude advantage of $S_Q^{\text{stag}}(\mathbf{k}^*)$ over the all-plaquette estimator establishes it as the standard probe for future bilayer kagome campaigns.

VII. CONCLUSION

We have characterised bilayer kagome spin ice on the D-Wave Advantage2 processor across a $4 \times 13 \times 14$ parameter grid reaching 1,536 logical spins, one of the largest frustrated quantum spin-ice systems studied on any quantum processor. The native two-group architecture of the Zephyr processor maps naturally onto two coupled kagome planes, providing bilayer geometry without additional embedding overhead and opening a second experimental axis, the interlayer coupling J_\perp , orthogonal to the quantum drive Γ_{eff} .

Three findings emerge from exploiting this geometry. Interlayer exchange drives a sharp, ground-state antiferroelectric Ice-II phase, signalled by the C_s^\perp sign reversal

at $(J_\perp/J_1)^* \approx 0.044$ and stable across five decades of annealing time; this phase has no classical or single-layer analogue and is the direct QPU counterpart of antiparallel monopole correlations predicted in bilayer Permalloy architectures. Restricting the charge structure factor to the ice manifold yields an order-of-magnitude enhancement over conventional all-plaquette probes, establishing $S_Q^{\text{stag}}(\mathbf{k}^*)$ as the correct estimator for any quantum spin ice experiment with non-negligible monopole density. The quantum renormalisation ratio $\rho_{\text{max}} = 0.2771$ converts the hardware gap into a concrete engineering specification, $\Gamma_c \gtrsim 0.6 J_1$, for the first quantum device to enter the monopole Coulomb phase.

Three falsifiable predictions, a critical vertical separation $d_z^* \approx 790\text{--}870$ nm, a monopole activation temperature $T^* \approx 580\text{--}720$ K in compressed bilayers, and an order-of-magnitude Ice-II signal enhancement in existing XMCD datasets, offer immediate experimental handles on these phases, all testable in the $\text{Ni}_{81}\text{Fe}_{19}$ nanowire geometry of Ref. [15] without new fabrication. As qubit counts grow and the $(\Gamma_{\text{eff}}, J_\perp)$ parameter space explored here scales to larger systems, the coupled-plane annealer architecture provides a natural and scalable route toward the quantum magnetic Coulomb phase in programmable spin ice.

-
- [1] C. Castelnovo, R. Moessner, and S. L. Sondhi, *Nature* **451**, 42 (2008).
 - [2] S. T. Bramwell and M. J. P. Gingras, *Science* **294**, 1495 (2001).
 - [3] G. Moller and R. Moessner, *Phys. Rev. B* **80**, 140409 (2009).
 - [4] N. Rougemaille and B. Canals, *Eur. Phys. J. B* **92**, 62 (2019).
 - [5] R. F. Wang, C. Nisoli, R. S. Freitas, J. Li, W. McConville, B. J. Cooley, M. S. Lund, N. Samarth, C. Leighton, V. H. Crespi, and P. Schiffer, *Nature* **439**, 303 (2006).
 - [6] S. Ladak, D. E. Read, G. K. Perkins, L. F. Cohen, and W. R. Branford, *Nat. Phys.* **6**, 359 (2010).
 - [7] E. Mengotti, L. J. Heyderman, A. F. Rodríguez, F. Nolting, R. V. Hügli, and H.-B. Braun, *Nat. Phys.* **7**, 68 (2011).
 - [8] A. Farhan, P. M. Derlet, A. Kleibert, A. Balan, R. V. Chopdekar, M. Wyss, J. Perron, A. Scholl, F. Nolting, and L. J. Heyderman, *Nat. Phys.* **9**, 375 (2013).
 - [9] C. Nisoli, R. Moessner, and P. Schiffer, *Rev. Mod. Phys.* **85**, 1473 (2013).
 - [10] D. J. P. Morris, D. A. Tennant, S. A. Grigera, B. Klemke, C. Castelnovo, R. Moessner, C. Czternasty, M. Meissner, K. C. Rule, J.-U. Hoffmann, K. Kiefer, S. Gerischer, D. Slobinsky, and R. S. Perry, *Science* **326**, 411 (2009).
 - [11] T. Fennell, P. P. Deen, A. R. Wildes, K. Schmalzl, D. Prabhakaran, A. T. Boothroyd, R. J. Aldus, D. F. McMorrow, and S. T. Bramwell, *Science* **326**, 415 (2009).
 - [12] C. Castelnovo, R. Moessner, and S. L. Sondhi, *Annu. Rev. Condens. Matter Phys.* **3**, 35 (2012).
 - [13] K. Kimura, S. Nakatsuji, J.-J. Wen, C. Broholm, M. B. Stone, E. Nishibori, and H. Sawa, *Nat. Commun.* **4**, 1934 (2013).
 - [14] R. Sibille, N. Gauthier, H. Yan, M. Ciomaga Hatnean, J. Ollivier, B. Winn, U. Filges, G. Balakrishnan, M. Kenzelmann, N. Shannon, and T. Fennell, *Nat. Phys.* **14**, 711 (2018).
 - [15] A. May, M. Hunt, A. Van Den Berg, A. Hejazi, and S. Ladak, *Commun. Phys.* **2**, 13 (2019).
 - [16] A. Farhan, C. F. Petersen, S. Dhuey, L. Anghinolfi, B. Luk'yanchuk, A. Scholl, L. J. Heyderman, and P. M. Derlet, *Sci. Adv.* **5**, eaav6380 (2019).
 - [17] A. D. King *et al.*, *Science* **373**, 576 (2021).
 - [18] A. Lopez-Bezanilla, A. D. King, J. Raymond, M. H. Amin, J. P. Hilton, T. Lanting, A. J. Berkley, W. A. Bernoudy, C. Coffrin, M. Dehn, *et al.*, *Nat. Commun.* **14**, 1105 (2023).
 - [19] M. Troyer and U.-J. Wiese, *Phys. Rev. Lett.* **94**, 170201 (2005).
 - [20] A. P. Ramirez, A. Hayashi, R. J. Cava, R. Siddharthan, and B. S. Shastry, *Nature* **399**, 333 (1999).
 - [21] A. A. Houck, H. E. Türeci, and J. Koch, *Nature Physics* **8**, 292 (2012).
 - [22] K. Ghosh, Universal quantum suppression in frustrated ising magnets across the quasi-1d to 2d crossover via quantum annealing (2026), arXiv:2603.24311 [cond-mat.str-el].
 - [23] L. Savary and L. Balents, *Phys. Rev. Lett.* **108**, 037202 (2012).
 - [24] S. Lee, S. Onoda, and L. Balents, *Phys. Rev. B* **86**, 104412 (2012).

Appendix A: Ergodicity diagnostics

The unique-configuration fraction $f_{\text{uniq}} = 1.0000$ at all (N, J_{\perp}, t_a) points throughout the sweep, as shown in Fig. 9. As discussed in Sec. VC, this saturation is expected from information-theoretic grounds and does not indicate the absence of thermalisation. Figure 10 shows the non-saturating ergodicity metrics d_H and H_s , which decay monotonically from fast to slow anneals and yield the characteristic collapse time $t_a^{\dagger} \approx 0.02 \mu\text{s}$ marking the onset of classical freezing.

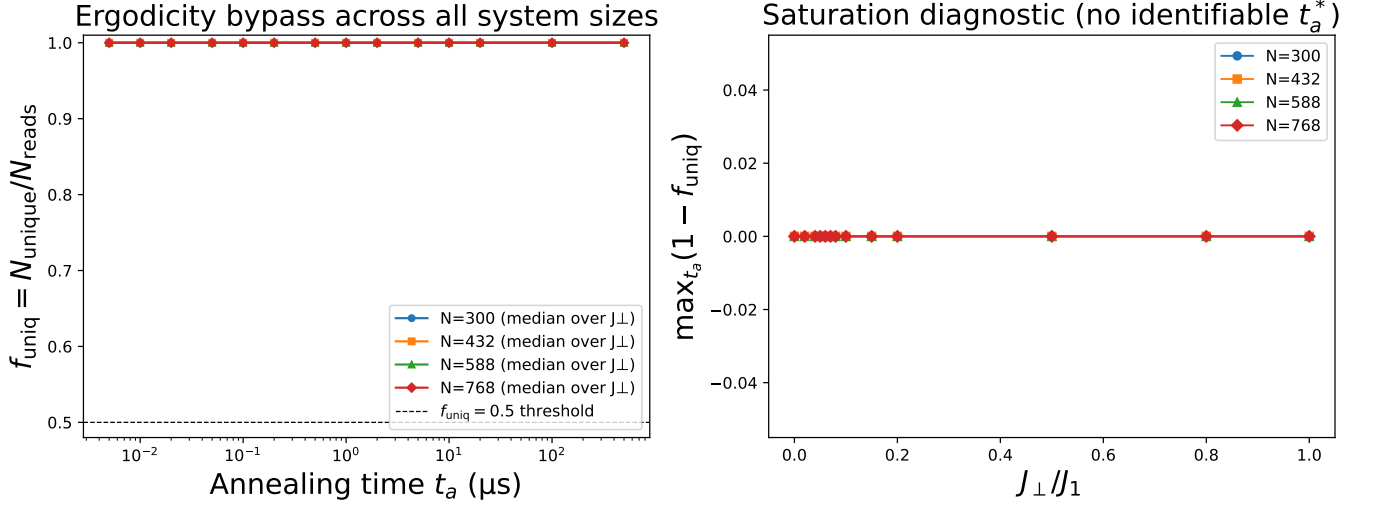


FIG. 9: Ergodicity bypass via unique-configuration fraction f_{uniq} . *Left*: Median f_{uniq} vs. t_a for each system size (shading: min-max band over all J_{\perp}). Universal saturation at unity is expected from the exponentially large ice manifold and does not indicate absence of thermalisation. *Right*: Fallback diagnostic $\max_{t_a}(1 - f_{\text{uniq}})$ vs. J_{\perp}/J_1 , confirming saturation across all couplings and system sizes.

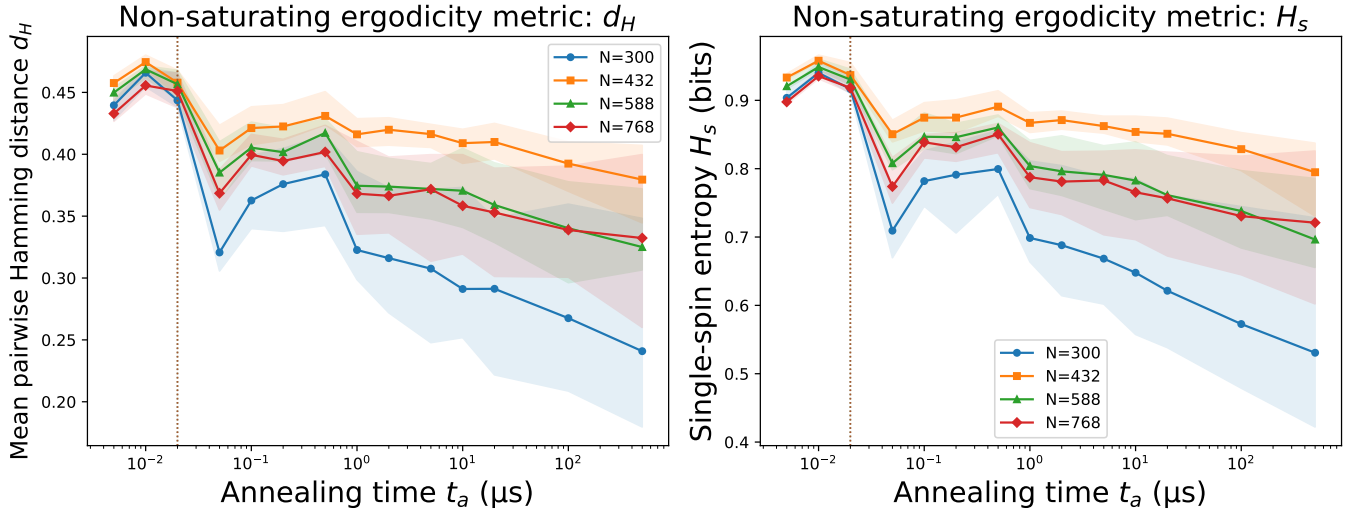


FIG. 10: Non-saturating ergodicity metrics. *Left*: Mean pairwise Hamming distance d_H (normalised by spin count) vs. t_a , decaying from ≈ 0.40 – 0.45 at fast anneals to ≈ 0.20 at slow anneals. *Right*: Single-spin entropy H_s (bits) vs. t_a , decaying from ≈ 0.90 – 0.95 to ≈ 0.65 – 0.70 . Characteristic collapse times $t_a^{\dagger} \approx 0.02 \mu\text{s}$, identified via the maximum of $|dd_H/d \ln t_a|$, are consistent across all system sizes and mark the onset of classical freezing.

Appendix B: Blind holdout validation

Figure 11 shows the full blind holdout validation of the C_m^\perp sign-change coupling, following the sequential protocol of Ref. [22]. Three near-critical couplings ($J_\perp/J_1 = 0.04, 0.05, 0.06$) and two farther stress-test couplings (0.2, 0.5) are withheld in turn. All five predicted crossings remain sub- 1σ ($\Delta/\sigma = 0.41\text{--}0.64$), confirming that the Ice-II onset is a smooth, continuous function of J_\perp/J_1 and ruling out a first-order interlayer reordering within measurement precision.

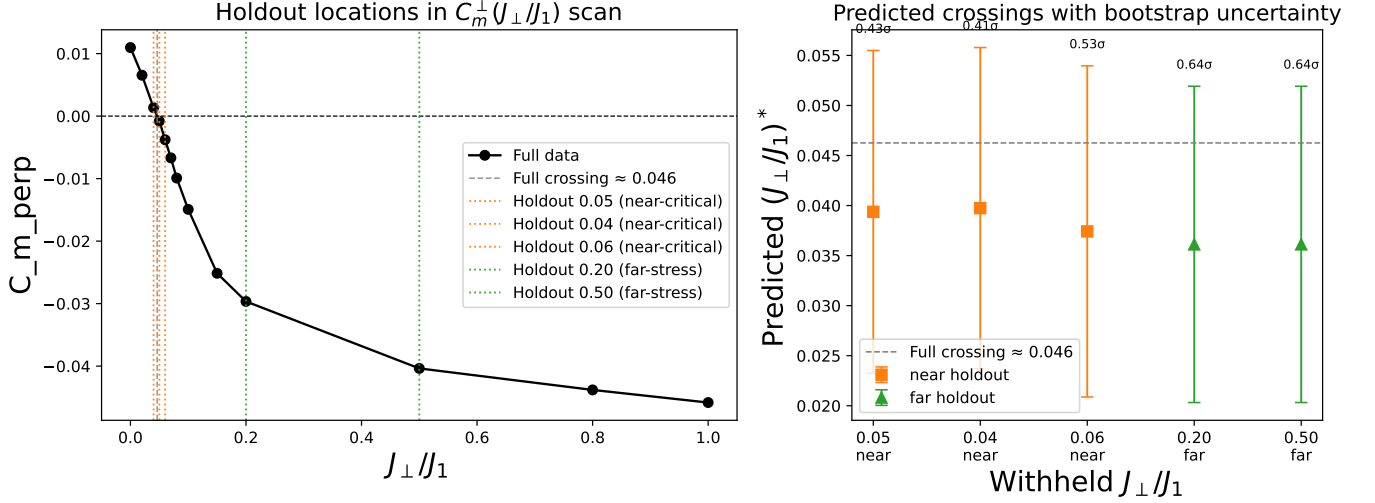


FIG. 11: Blind holdout validation of the Ice-II onset coupling. *Left:* $C_m^\perp(J_\perp/J_1)$ at $t_a = 500 \mu\text{s}$ with three near-critical holdouts ($J_\perp/J_1 = 0.04, 0.05, 0.06$) and two farther stress-test holdouts (0.2, 0.5). *Right:* Predicted crossings from retained-data fits with bootstrap uncertainties; all five tests remain sub- 1σ ($0.41\sigma\text{--}0.64\sigma$), supporting a smooth crossover and disfavoring a first-order bilayer transition.